PHYSICAL REVIEW B VOLUME 31, NUMBER 2 15 JANUARY 1985

# Heat capacity of antimony pentachloride—intercalated graphite

Donald N. Bittner* and Michael Bretz
*Department of Physics, University of Michigan, Ann Arbor, Michigan 48109*
(Received 11 June 1984)

We have measured the heat capacity of several $SbCl_5$-intercalated highly oriented pyrolytic graphite samples between 10 K and room temperature with ac-calorimetry techniques. The data are analyzed for low-$T$ lattice modes, molecular rotation effects, and intramolecular vibrational modes. We find evidence for rotational unbinding in some samples near 150 K and an activation process commencing at the 220-K disordering transition, while stage-2 samples prepared by immersion in liquid $SbCl_5$ show first-order transitions at 220 K. Our measurements support the occurrence of $SbCl_3$ dimerization suggested by recent x-ray-scattering measurements of antimony chloride graphite intercalation compounds.

## I. INTRODUCTION

We report ac heat-capacity measurements taken on stage 2 to 6 antimony pentachloride—intercalated highly oriented pyrolytic graphite (HOPG) samples between 10 K and room temperature. This study complements the growing experimental literature on these acceptor-type graphite intercalation compounds (GIC's). Briefly, $SbCl_5$ is one of several metal halides which are readily intercalated between the weakly attracting graphite lamina.[1] High-temperature staging transitions[2] allow relatively pure-stage macroscopic samples to be prepared under proper conditions of temperature and pressure.[3] Unlike most acceptor GIC's, the $SbCl_5$ intercalates are air stable,[4] which allows for handling and accessory mounting.

There is evidence that $\gtrsim 70\%$ of the $SbCl_5$ molecules disproportionate upon intercalation. Mössbauer studies[5] found two main spectral lines corresponding to $Sb^{5+}$ and $Sb^{3+}$ atomic states of intercalant. The $Sb^{5+}$ Mössbauer line position suggests that $SbCl_6{}^-$ is the dominant species, while the relative Mössbauer peak areas give $1.9\pm0.1$ for the $[SbCl_6{}^-]/[SbCl_3]$ ratio. The compound's stoichiometry can be determined by $c$-axis x-ray diffractometry. Boca *et al.*,[6] through a careful diffraction analysis, corroborated the disproportionation reaction

$$3SbCl_5+2e^- \rightarrow 2SbCl_6{}^- + SbCl_3 , \qquad (1)$$

which takes place upon intercalation, and gave evidence for bridging of constituent molecules between the confining graphite lamina.

In-plane x-ray-diffraction studies at room temperature have revealed that the intercalant forms a $(\sqrt{7}\times\sqrt{7})R(\pm19.1^\circ)$ ordered lattice,[3] while in-plane electrical-resistivity measurements[7] showed an unexplained "bump" at 230 K. Further detailed x-ray and resistivity work by Clarke *et al.*[8,9] found that this feature is due to an ordering transition to a segregated, nearly commensurate $(\sqrt{39}\times\sqrt{39})R(\pm16.1^\circ)$, low-temperature superlattice in stage 2 to 6 $SbCl_5$ GIC's. Considerable hysteresis in resistivity indicated first-order behavior, and x-ray evidence for a crossover from three-dimensional (3D) correlations of stage-1 GIC's to quasi-2D correlations for stage-3 GIC's suggests a lower-dimensionality transition.[9]

Electron-microscopy studies of liquid-immersion-prepared single-crystal and HOPG $SbCl_5$ stage-2 intercalates[10] confirm the $\sqrt{7}\times\sqrt{7}$ and $\sqrt{39}\times\sqrt{39}$ structures as well as the $\sim$220-K transition. (In Ref. 10 an additional low-temperature ring pattern superimposed on the $\sqrt{7}\times\sqrt{7}$ electron-scattering peaks is interpreted as a glassy phase.) Also, no changes were seen in the position and width of the 1631- and 1615-$cm^{-1}$ Raman lines when crossing the low-$T$ phase transition.[10] A $(00l)$-lattice fringe-imaging method showed "large ($600\times2000$ Å$^2$) well-staged, defect-free regions."[10] Other experimental work on the properties of $SbCl_5$ GIC's at room temperature and below include the analysis of phonon-dispersion modes,[5] Raman scattering of high-frequency interlayer modes,[11,12] and transport properties down to 2 K.[13] Some excellent recent reviews of GIC's are also available.[14]

Because interesting low-$T$ behavior has been demonstrated for $SbCl_5$ intercalates, we chose to measure the heat capacity of several intercalated HOPG samples. We used an ac-calorimetry technique on small ($0.5\times0.5\times10$ mm$^3$) samples prepared both by liquid-immersion (one zone) and vapor-phase (two zone) intercalation procedures. ac techniques and resultant heat-capacity data are presented fully in the following sections.[15] During the course of this experiment a new exhaustive x-ray study of the structural transitions in antimony chloride graphite compounds was completed by Homma.[16] He identified the low-$T$ phase ($\lesssim 220$ K) as an incommensurate $\sim$3.7% compressed $\sqrt{39}\times\sqrt{39}$ structure coexisting with a commensurate $\sqrt{7}\times\sqrt{7}$ superlattice, and the high-$T$ disordered phase as fluidlike. Homma interpreted the transition as a low-temperature dimerization of $SbCl_3$ molecules with oppositely paired dipole moments. Rayment *et al.* also interpret their x-ray powder-diffractive measurement as being consistent with polymerization.[17]

## II. EXPERIMENTAL PROCEDURES

### A. ac heat-capacity technique

We used a steady-state ac-calorimetry technique first developed by Sullivan and Seidel in 1966 for measuring small samples.[18] As shown in Fig. 1, a sample with internal heat capacity $C_s$ and thermal conductance $K_s$ is connected to the temperature bath $T_b$ through a weak thermal link having conductance $K_b$. The attached heater and thermometer are chosen to maximize the contact conductances $K_H$ and $K_\theta$, and to minimize the heat capacities $C_H$ and $C_\theta$. When an ac voltage of frequency $\omega\sqrt{2}$ is applied to the heater, the sample rises above $T_b$ and oscillates about a steady-state offset temperature. The magnitude of these oscillations, $T_{\text{ac}}$, depends on $\omega$, the various thermal time constants $\tau_i = C_i/K_i$, and the sample heat capacity $C_s$ through the relation

$$T_{\text{ac}} = \frac{P}{\sqrt{2}\omega C_s}[1+(\omega\tau_1)^{-2}+(\omega\tau_2)^2]^{-1/2} . \quad (2)$$

Here, $P$ is the power to the heater with frequency $\omega$, and $\tau_1$ and $\tau_2$ are the weak-link and effective internal-cell time constants, respectively. $T_{\text{ac}}$ is shifted out of phase by an amount

$$\alpha \simeq \arcsin\{1+[(\omega\tau_1)^{-1}-\omega\tau_2]^2\}^{-1/2} . \quad (3)$$

One always measures the frequency profile to determine an operating frequency within a "plateau" region where neither $\tau_1$ nor $\tau_2$ dominate $T_{\text{ac}}$. For frequencies on the plateau, Eq. (2) simplifies to

$$T_{\text{ac}} \cong P/\sqrt{2}\omega C_s , \quad (4)$$

from which the heat capacity $C_s$ can be easily calculated. In practice, the weak link, heater, thermometer, and addenda must be chosen carefully to match the thermal-diffusion lengths, $l_i = (2\kappa_i/\omega\rho_i c_i)^{1/2}$, of each material of the ac cell (where $\rho$ is the density, $\kappa$ is the thermal conductivity, and $c$ is the specific heat). The appropriate operating frequency can be determined by scanning $\alpha$ and $\omega T_{\text{ac}}$ and can be maintained by monitoring $\alpha$ to ensure that one has not shifted off the plateau.

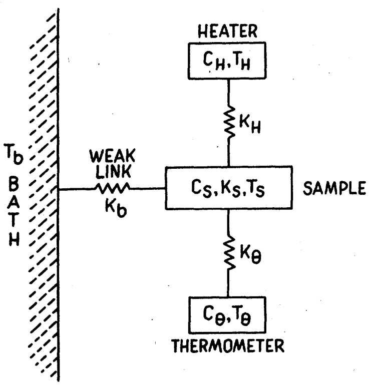

FIG. 1. Idealized ac heat-capacity sample and addenda.

All phase-transition features of our study are delineated by the ac heat-capacity method. For a singularity, the thermal wavelength, which is proportional to $1/C_s$, would go to zero, resulting in an internal decoupling of the cell, which, in turn, would reduce the measured heat capacity. We estimate that heat capacities must be an order of magnitude larger than those measured here before significant internal thermal decoupling would take place.[19] Any abrupt heat capacity change would also show up as a change in the phase of $\alpha$. We monitored $\alpha$ continuously and found it always to be well behaved. Sharp heat-capacity features are smoothed by an amount $T_{\text{ac}}$, the amplitude of temperature oscillations. Our $T_{\text{ac}}$'s were typically 10 mK with data temperature increments of 0.5 K.

### B. Sample preparation and measurement techniques

The HOPG samples were potted in Formvar and cut to $0.5\times0.5\times10$ mm$^3$ with a jeweler's saw. After light sanding and unpotting in dichloroethane, the samples were washed in nitric acid and rinsed for 10 min in water before air drying. They were sealed in glass tubes containing antimony pentachloride and heated for 6—12 h. Some stage-2 intercalation samples were obtained with the HOPG immersed directly in the $SbCl_5$ liquid (one-zone method) and heated to 200 °C. Stages 2 through 6 were prepared by a two-zone method in which samples at 180—200 °C only contacted the $SbCl_5$ vapor from liquid heated differentially to 120—170, 100—110, 80—95, 40—60, and $\sim$20 °C, respectively. Staging was subsequently determined from $(00l)$ scans on a Mo $K\alpha$ x-ray diffractometer.[16] Heaters were $\sim$100-$\Omega$ gold films vapor-deposited onto $\lesssim$0.1-mil Mylar strips. Thermometers were flash-evaporated $Ge_{0.82}Au_{0.18}$ mixtures[15] which were annealed at 120 °C to obtain resistors of $\sim$80 k$\Omega$ whose resistance $R$ varies with temperature as $\approx T^{-0.6}$. The Mylar heater and thermometer strips were mounted with Formvar on opposite edges of the sample perpendicular to the crystallographic $a$ axis. Four 2-mil copper wires were attached with silver paint for electrical contacts. They also served as the thermal weak link to the temperature bath. The cell was placed in a vacuum chamber and helium exchange gas was admitted when necessary to provide thermal clamping to the cryostat temperature platform. The cell electrical leads were attached to larger copper wires leading to the posts of a vacuum-chamber feedthrough. Platinum- and germanium-calibrated resistance thermometers were used to calibrate each sample thermometer from room temperature to 4 K. The thermometers were driven by a constant-current source ($\pm$0.1%) through a precision resistor which supplied 14 $\mu$A for operation above 48 K and 4 $\mu$A for lower $T$. The heater obtained its power from a Krohn-Hite model 4100A oscillator and precision resistor, and a vector lock-in amplifier (Princeton Applied Research model 129A) was used to measure the voltage drop across the heater. The voltage drop $V_{\text{ac}}$ across the thermometer was monitored and related to $T_{\text{ac}}$ through the relation $V_{\text{ac}} = I(dR/dT)T_{\text{ac}}$, where $I$ is thermometer current. The ac voltage and phase measurements were

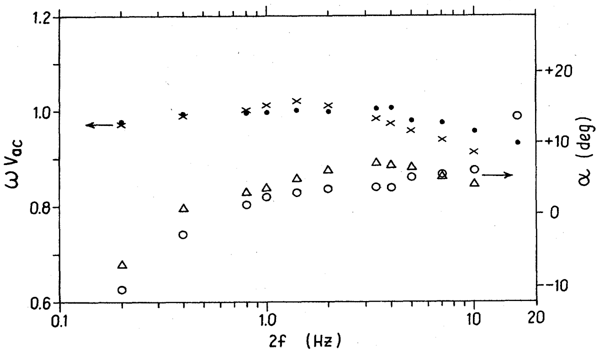

FIG. 2. Frequency scans for a stage-4 sample. $\omega V_{\rm ac}$ is normalized to its maximum value. Symbols refer to scans taken at 273 K (× and △) and at 77 K (● and ○).

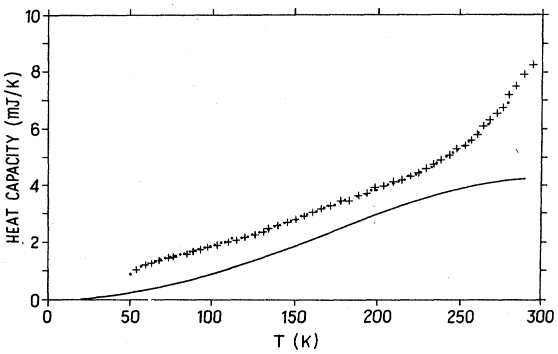

FIG. 3. Fitted graphite and copper heat-capacity contributors to stage 3, sample (1). Both warming (●) and cooling (+) data are shown.

performed using an Ithaco model 393 vector lock-in amplifier in the $2f$ mode. Signals were fed through a 12-bit, 16-channel analog-to-digital converter board to a Cromemco microcomputer for data reduction and analysis. Typical frequency scans at room temperature and at 77 K are shown in Fig. 2. A $\omega T_{\rm ac}$ plateau extends above 1 Hz, so an operating $2f$ frequency of $\frac{1}{2}$ Hz was chosen for all temperatures. The phase at the output of the lock-in amplifier (uncorrected for electronic internal phase shifts) is also given in Fig. 2.

### C. Data-reduction procedures

Data were taken while the cell was either cooling or warming slowly. The computer recorded several voltages at operator-specified temperature increments and then calculated the heat capacities. Typical warm-ups from 48 to 280 K took nearly 36 h, while cool-downs took about 15 h. The warm-up from 4.2 to 60 K took an additional 12 h. The heat capacity of unintercalated HOPG samples were measured first and fitted to the published heat capacities of copper[20] and graphite[21] from 40 to 280 K. The calculated weights of graphite from the fits agreed within 5% to actual HOPG-sample weights, but the copper contributions were always greater than the masses of the lead wires. Evidently, there is a contribution from the larger copper wires to which the weak links were attached. The fitted mass of copper along with actual sample graphite masses were used in subtracting a background contribution from the total heat capacities of the GIC's. Figure 3 shows the total heat capacity and background (solid curve) for a stage-3 sample. This sample has the largest ratio of background to total signal of all samples tested. More typically, the background constitutes $\frac{1}{2}$ of the total heat capacity.

Tests were performed on samples to check for variations due to cycling and time evolution. Data taken during cooling and warming are identical to those seen in Fig. 3. Hysteresis was only found in samples prepared by the one-zone method (to be presented later). A stage-2 sample was warmed about twice as fast and cooled twice as slowly as typical cycle times (indicated previously), but no differences were found. It was then quenched to 77 K in about 15 min and warmed back to 191 K over 2 h, after which time variations in the heat capacity were monitored by taking data at constant $T$ for $7\frac{1}{2}$ h. The heat capacity was constant within ±1% scatter. After taking heat-capacity and x-ray measurements, nine GIC samples were deintercalated by heating in vacuum to $\gtrsim 900\,^{\circ}\mathrm{C}$ for $1\frac{1}{2}$—2 h. Their mass changes upon exfoliation, given in Table I, were used to calculate the relative density, which is number of carbon atoms per $\mathrm{SbCl_5}$ molecule divided by stage. Relative densities for stages 3—5 are close to 14, as expected from $\mathrm{C}_{14n}\mathrm{SbCl}_5$. Masses for the stage-2 and -6 samples, however, deviated appreciably from this value for reasons which are not apparent. The graphite content of samples not subsequently exfoliated and weighed was calculated by averaging the relative densities for other samples of that stage.

### D. X-ray characterization of the samples

The heat-capacity samples have been characterized with x-ray diffraction using a $\lambda=0.7107$ Å Mo $K\alpha$ source. The stage-2 $(00l)$ x-ray profiles for one- and two-zone-prepared samples are given in Fig. 4. Staging is determined from peak positions through the Bragg condition $m\lambda=2d\sin\theta$, where $\theta$ is the scattering angle, $d$ is the stage spacing, and $m$ is the order number. We found good staging with less than 1% stage-3 content. Further scans (not shown) also found trace fractions of the next-higher stage to be present. The one-zone-sample peaks are a little sharper and higher-order peaks are a little larger than for the two-zone sample, indicating somewhat better stage uniformity. Recent structural calculations of Homma[16] reveal that the ratio of the two largest peaks is a measure of the $[\mathrm{SbCl_6^-}]/[\mathrm{SbCl_3}]$ concentration, and that the ratio of the strongest peak to the peak at $2\theta\sim25^{\circ}$ is linearly related to the relative intercalate density. Table I contains the x-ray determination of these ratios.

The disproportionation fractions are close to 2, the expected value of the disproportionation reaction for intercalated atoms. However, significantly, the relative densities are all clustered together near a value of 20, which is somewhat more dilute than the ideal stoichiometry. We believe that this difference reflects a *less uniform* inter-

TABLE I. Sample weight, intercalant content, and relative density. ND means that no data were taken for these samples.

| Sample: Stage, (no.), and (group) | Total mass (mg) (intercalated) | Graphite mass (mg) (exfoliated) | Relative density (by weight) | Relative density (by x rays) | Disproportionation fraction $[SbCl_6^-]/[SbCl_3]$ |
|---|---|---|---|---|---|
| Stage 2-(1) | 12.8 | 7.60 | 18.2 | 20 | 1.2 |
| -(2) | 14.1 | | | 20 | 1.2 |
| -(3)(*C*) | 16.8 | | | | |
| -(4)(*C*) | 15.1 | | | | |
| Stage 3-(1)(*B*) | 13.6 | 8.45 | 13.6 | 19 | 2.4 |
| -(2)(*B*) | 4.4 | | | | |
| -(3)(*A*) | 7.1 | | | | |
| -(4)(*A*) | 7.1 | | | | |
| -ND | 10.2 | 6.22 | 13.0 | | |
| -ND | 7.4 | 4.50 | 12.9 | | |
| Stage 4-(1)(*B*) | 7.1 | 4.75 | 12.6 | 21 | 2.4 |
| -(2)(*B*) | 10.3 | 6.81 | 12.2 | | |
| -ND | 19.5 | 12.97 | 12.4 | | |
| Stage 5-(*B*) | 27.0 | 19.50 | 13.0 | 20 | 2.8 |
| Stage 6-(*A*) | 20.6 | 12.51 | 6.4 | 22 | 2.6 |

calation process for our HOPG samples than for most of Homma's single-crystal graphite intercalants,[16] even though the *a*-axis widths of our samples are typically 0.5 mm, while Homma's are 5-mm squares. These small relative intercalant densities, when compared with weighing (see Table I), indicate an *incomplete* equilibrium of the intercalation reaction.

In-plane room-temperature x-ray scans were performed on the stage-2 samples as shown in Fig. 5. The broad diffuse background has been identified by Homma[16] as a fluidlike phase consisting of $SbCl_3$ molecules. X-ray diffraction from two-zone samples shows a single peak above the diffuse background at the $\sqrt{7}$ (100) position calculated from the Bragg condition. This agrees with previous x-ray determinations of stage-2 behavior where the $\sqrt{7}\times\sqrt{7}$ phase is present at room temperature with a commensurate-incommensurate transition occurring near 340 K.[22] In contrast, the in-plane scan for the one-zone sample displays additional well-developed peaks at positions of the $\sqrt{39}$ structure. This is entirely unexpected and constitutes the first observation of a room-temperature stable $\sqrt{39}\times\sqrt{39}$ structure in $SbCl_5$ GIC's. The 2D domain sizes of the ordered phases are inversely related to the x-ray linewidths. For the $\sqrt{7}\times\sqrt{7}$ $SbCl_6^-$ solid, we find 100-Å domains; for the $\sqrt{39}\times\sqrt{39}$ $SbCl_3$ phase we obtain $\gtrsim$165-Å (resolution-limited) islands. Further in-plane scans were performed at 240 and 170 K. We found no relative peak shifts or additional peaks for this one-zone-prepared sample.

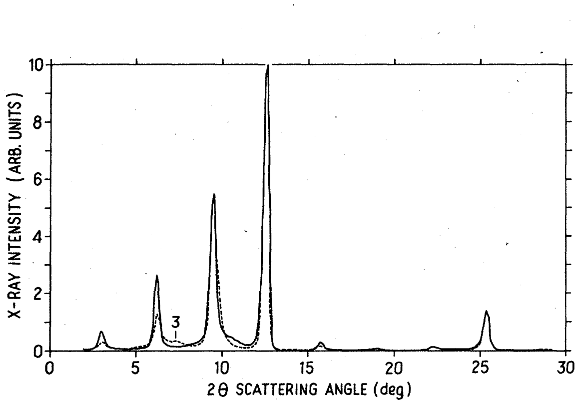

FIG. 4. X-ray-diffraction (00*l*) scan of the stage-2, one-zone sample (3) (solid line) and stage-2, two-zone sample (1) (dashed line). Trace stage-3 presence is indicated.

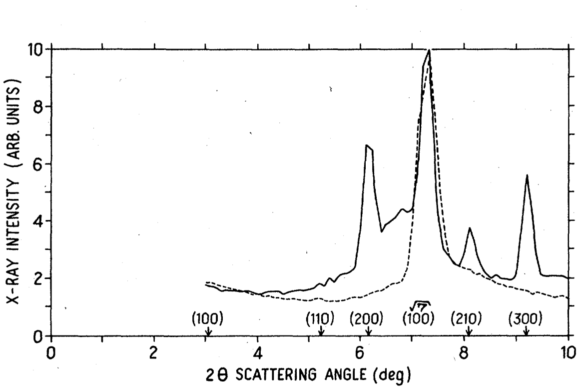

FIG. 5. In-plane room-temperature x-ray scans for stage-2, one-zone, sample (1) (solid line) and stage-2, two-zone, sample (3) (dashed line). Calculated Bragg reflection rings for $\sqrt{39}\times\sqrt{39}$ structure are indicated by arrows.

## III. PRESENTATION OF THE SPECIFIC-HEAT DATA

The specific-heat capacities of all our samples are presented in Figures 6—8. Background contributions were subtracted off before dividing by intercalant content (from Table I) to give the specific heats. Data below 80 K were taken for about half of the samples. Measurements above room temperature were not possible because the corrosive intercalant would rapidly degrade our heaters and thermometers. The data, obtained for rising temperature unless otherwise noted, were arbitrarily separated into groupings which we feel best illustrate some important similarities among the various samples. Data groups *A* and *B*, shown in Fig. 6 and Fig. 7, respectively, are for two-zone-prepared samples, while data group *C* (Fig. 8) gives our measurements for stage-2, one-zone-prepared samples. In discussing the data, we will avoid ambiguity by occasionally designating stage *n*, sample (*m*) as belonging to its group [i.e., stage 4*B*-(2) in Table I]. The accuracy of our background-subtraction corrections is approximately $1k_B$. For clarity, some data points have been deleted from the figures.

Group *A* can be characterized as having essentially monotonic specific heats with increasing temperature. These specific heats are quite large, indicating that many molecular degrees of freedom are contributing to the total signal. There is a low-temperature feature in the stage-6 data at 45 K, and some subtle changes in one stage-3 sample at 115 K. Above about 200 K the specific heats for all samples rise more strongly with *T*, signaling some type of activation process. It is significant that this feature commences where the $\sqrt{39}\times\sqrt{39}$ disordering transition is expected. A distinct shoulder is also evident in one stage-3 sample at 230 K. (The solid lines in Fig. 6 will be discussed later.)

The group-*B* curves of Fig. 7 rise monotonically at low temperatures, just like the group-*A* data with stage 5 overlapping stage 6 of group *A* and stage 4*B*-(2) following the stage-3*A* specific heats. However, at about 150 K, plateaus appear in the group-*B* data. These extend in temperature up to ~220 K, where activation processes commence. The plateau heights, except for stage 4*B*-(1), which only hints of 150-K activity, are equally spaced at $(7-8)k_B$. They are also stage dependent with higher stages possessing lower specific heats. The group-*A* data show a similar trend. The lower curve, stage 3*B*-(1), is anomalous in possessing an essentially temperature-independent plateau spanning 160 K whose height is much below the other stage-3 specific heats.

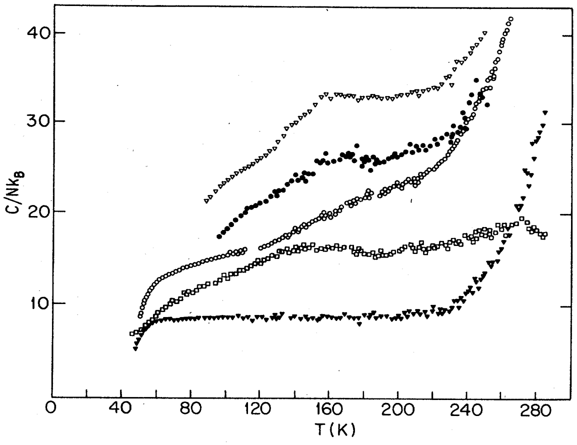

FIG. 7. Group-*B* specific heats. Stage 3*B*-(1), ▼; stage 3*B*-(2), ∇; stage 4*B*-(1), ○; stage 4*B*-(2), ●; and stage 5, □.

Stage-2 samples prepared by the two-zone method were also measured, but are not shown. Sample 2-(1) overlaps the stage-4*B*-(1) sample below 150 K and follows stage-5 specific heat at higher *T*. As in the stage-5 sample, the activation contribution above 220 K is very weak. Stage 2-(2), on the other hand, overlaps stage 5 at low *T*, then follows stage 4-(1) above 150 K. At 200 K, a discontinuity appears after which the specific heat diverges strongly.

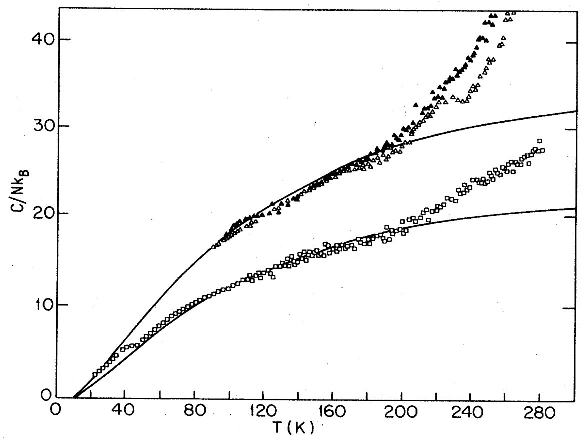

FIG. 6. Group-*A* specific heats for stage 6, □; stage 3*A*-(3), △; and stage 3*A*-(4), ▲. The vibrational specific heats for SbCl$_5$ calculated from Fig. 9 is multiplied by factors of 2 (lower line) and 3 (upper line).

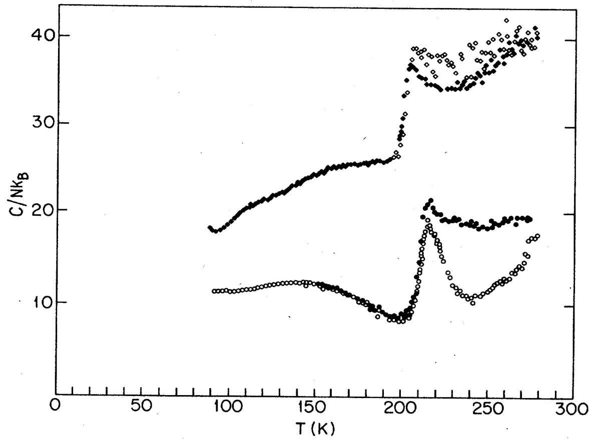

FIG. 8. Group-*C* specific heats of one-zone-prepared samples. Stage 2*C*-(3), ◇; stage 2*C*-(4), ○. Solid symbols denote cooling.

Group-*C* data, which are shown in Fig. 8, consist of two one-zone-prepared stage-2 samples. The specific heat of the sample 2*C*-(3) is identical to that of stage 4*B*-(2) up to 195 K, where it rises abruptly, *signaling a phase transition.* The temperature region above this transition displays considerable hysteresis, indicative of a first-order phase change. Near 260 K, the hysteresis has disappeared and the specific heat seems to have returned again to the stage-4*B*-(2) curve. The specific heat of the other one-zone sample, 2*C*-(4), is similar to 2*C*-(3) in possessing a strong first-order phase transition (although with considerably more hysteresis). The transition temperature, however, appears to be about 10 K higher in than 2*C*-(3). The low-temperature specific heat is about constant, while above 150 K it descends toward the lower plateau of 3*B*-(1) before the phase transition brings the specific heat to the two-zone stage-2-(1) value.

## IV. ANALYSIS

In this section we shall propose several mechanisms which should contribute to the intercalant specific heat. Intramolecular vibrations, lattice modes, rotational states, and the observed high-$T$ activation will be discussed, followed by an analysis of the group-*C* first-order transition at 220 K.

### A. Intramolecular vibrations

The intramolecular vibrational heat-capacity contribution for intercalated $SbCl_3$ and $SbCl_5$ should be comparable to that for 3D gas, with crystallization due to van der Waals forces only causing perturbations.[23] However, hydrogen-bonded or -ionized molecules could have appreciably shifted spectra, so estimates of $SbCl_6^-$ vibrational modes are not appropriate. The low-frequency Raman- and infrared-active modes of $SbCl_3$ (Ref. 24) and $SbCl_5$ (Ref. 25) are given in Table II along with their degeneracies. These comprise the $3n$-6 possible modes for the $n$ atoms of each molecule. The specific heats, calculated from the Einstein model of harmonic oscillators, are given in Fig. 9. The thermal activity of $SbCl_5$ is more than twice that for $SbCl_3$ due to the larger number of doubly degenerate low-temperature vibrational modes. Since the ideal disproportionation reaction gives only one $SbCl_3$ molecule for each two $SbCl_6^-$ molecules, the vibrational specific-heat contribution of $SbCl_3$ will be rather small in these GIC's. However, if $SbCl_6^-$ behaves thermally at all like $SbCl_5$, the vibrational heat-capacity contribution can be sizable below room temperature. No specific-heat measurements have been reported for bulk $SbCl_5$, but constant-pressure specific heats for other inorganic halides are about $C_p/Nk_B \approx 25$—29 at room temperature.[26] This is about twice our calculated vibrational contribution.

TABLE II. Vibrational frequencies of $SbCl_3$ and $SbCl_5$.

| Molecule | Frequency (K) | Degeneracy |
|---|---|---|
| $SbCl_3$ | 184 | 2 |
| | 236 | 1 |
| | 512 | 2 |
| | 542 | 1 |
| $SbCl_5$ | 107 | 2 |
| | 225 | 1 |
| | 239 | 2 |
| | 262 | 2 |
| | 442 | 1 |
| | 512 | 1 |
| | 551 | 1 |
| | 574 | 2 |

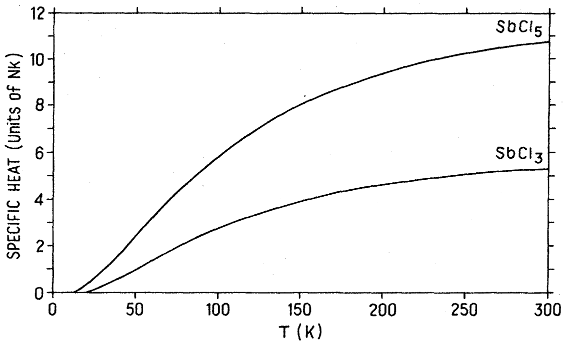

FIG. 9. Vibrational specific heats of $SbCl_3$ (lower curve) and $SbCl_5$ (upper curve) calculated from vibrational modes given in Table II.

We have matched our group-*A* specific heats with multiples of the calculated $SbCl_5$ vibrational activity. The lower and upper lines of Fig. 6 represent the specific-heat curves of bulk $SbCl_5$ (Fig. 9), which have been multiplied by 2 and 3, respectively. These fits are sufficiently close to our data that they will be used during the analysis of our low-$T$ specific-heat features. The fits shown in Fig. 6 indicate that the $SbCl_6^-$-ion vibrational modes are much like those of $SbCl_5$. If so, the extra electron causes a degeneracy doubling for stages 4*A*-(1), 5, and 6, and a degeneracy tripling for stages 2*C*-(3), 3*A*-(3 and 4), and 4*B*-(2). An integer multiplier of modes might arise from the interaction of ions with their images in the graphite lamina. Another possibility is that the $SbCl_3$ has polymerized, thereby creating a number of new internal vibrational modes, which raises the specific heat substantially.

### B. Intercalant-graphite interactions

Intermolecular vibrational modes are also present. These will overwhelm the linear electronic heat capacity which we ignore at the relatively high temperatures of this experiment. For both donor and acceptor GIC's, a low-energy dispersionless optical in-plane lattice shear mode is expected. Al-Jishi and Dresselhaus constructed a lattice-dynamical model for donor GIC's.[27] They calculate density-of-states anomalies below a frequency of 100 $cm^{-1}$ for stage-1—4 rubidium intercalates. A heat-capacity anomaly with a Schottky level of $\Delta = 34$ K was fitted with lower-temperature data by Mizutami *et al.* for stage-3—6 cesium intercalates,[28] and Suganuma *et al.* later found an Einstein anomaly with a $\Delta$ value of 51 K for the higher-stage rubidium compounds.[29] Alexander *et al.* measured the behavior for stage-1 Rb and Cs intercalates in the range 0.5—90 K.[30] All intercalate molecules appear to participate in these modes, whose characteristic temperatures are stage independent above stage 1. Inelastic-neutron-scattering experiments in stage-2 and -4 $SbCl_5$ GIC's (Ref. 31) show that the graphite-intercalant force constants are weaker for $SbCl_5$ than for the donor compounds. Thus we expect $\Delta$ for the *c*-axis longitudinal-phonon modes to be lower than found for the above studies.

We analyze the low-temperature activity of our GIC's after subtracting off twice the calculated vibrational specific heat of bulk $SbCl_5$ (lower curve in Fig. 6) from selected data sets of Figs. 6 and 7. This difference is plotted versus $T$ in Fig. 10 for stages 2, 4, and 5. Stages 2—4 possess a strong Schottky-type peak which diminishes to only a remnant for stages 5 and 6. A calculated specific heat for a two-level Schottky peak with $\Delta = 90$ K and degeneracy of 1 is shown for comparison (solid line in Fig. 10). Its height was magnified by a factor of 13.6 to bring it into agreement with the stage-2 data. This factor is close to the relative density of Table I and indicates that the anomaly is associated with additional graphite modes arising from the presence of the intercalant molecules. Contrary to expectations, $\Delta$ is larger than that for the donor compounds and is stage *dependent.* The $\Delta$ of 90 K for stage 2 becomes about 135 K for stages 3 and 4, and rises to some 155 K for stages 5 and 6. We note that the lowest-temperature stage-2 data lie well above the Schottky fit. It is therefore possible that the optical shear mode does occur where expected, and that the Schottky anomaly is a further excitation unique to $SbCl_5$ GIC's. We do not, as yet, understand this lattice-mode behavior.

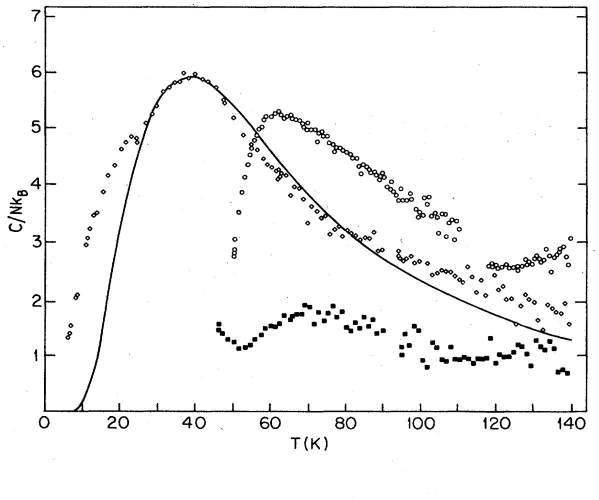

FIG. 10. Low-temperature specific heats after subtracting off 2× bulk $SbCl_5$ vibrational contribution. Stage 2-(1), ◇; stage 4*B*-(1), ○; and Stage 5*B*, ■. Solid line is 13.6× the specific heat of a two-level Schottky system with a level spacing of 90 K.

### C. Rotational specific heat

Molecular rotational levels of large molecules are excited at very low $T$ since the characteristic temperatures depend inversely on the moment of inertia. For $SbCl_5$ the gaseous rotational levels are fully excited by 1 K. However, we do expect these body rotations to be hindered appreciably by the graphite corrugation potentials. Although well-depth energies for chlorine on or in graphite are not available for modeling, molecules of similar size and shape as $SbCl_5$ are rotationally hindered when adsorbed on graphite. Pentacarbonyl, $Fe(CO)_5$, is an example of a bipyrimidal adsorbed molecule with a mass close to $SbCl_3$. Mössbauer and neutron-scattering studies[32] indicate not only significant rotational hinderance, but an orientational transition near 150 K just below melting for that compound.

Rotationally hindered molecules have a torsional vibrational energy of $1k_BT$ per mode at low temperature, where the angular motion is restricted. As the temperature increases, the molecules eventually gain enough energy to overcome their internal or external barriers and begin rotating. For high $T$ they become free rotors having $\frac{1}{2}k_BT$ per rotational mode. Thus, the rotational heat capacity for such molecules actually *decreases* with increasing temperature. We interpret the plateaus of group $B$ which commence near 150 K as a heat-capacity loss from the monotonically rising group-$A$ behavior. Below this temperature there are only vibrational and lattice modes, while over an extended temperature region above 150 K the specific heat begins to include rotational effects. The slope of the specific heat changes abruptly at 150 K, which indicates a collective unbinding process. The x-ray-diffraction studies find no rotational effects in the temperature region studied ($T \gtrsim 90$ K),[16] but these would be difficult to see since the rotational unbinding evidently occurs over such a wide temperature region. Hwang and Nicolaides do report low-temperature attenuation coefficients $\alpha_T$ for *c*-axis transverse sound propogation in $SbCl_5$ HOPG GIC's.[33] For samples well annealed at 207 K (data set $E$ in Ref. 33), the attenuation is constant at low $T$, but begins to rise near $\sim 150$ K, and after $\sim 200$ K it grows rapidly and finally diverges at the disordering transition. For samples annealed below 200 K, the *c*-axis shear elastic constant $C_{44}$ is large and drops gently with rising $T$, but then falls much more rapidly above $\sim 150$ K. Hwang and Nicolaides give evidence for the growth of $SbCl_3$ islands, and interpret the divergence in $\alpha_T$ and associated disappearance of $C_{44}$ as being due to melting of these 2D islands. They specify that island-boundary movement causes energy loss as measured by $\alpha_T$ and loss of shear rigidity as measured by $C_{44}$. For this movement to be appreciable, the dimers need to surmount the intramolecular and lateral substrate barriers which constrain molecular rotations and molecular mobility, respectively. Thus the temperature correspondence between our plateau formation at 150 K and features in the ultrasonic measurements is understandable. We should emphasize that our extremely slow cool-down procedure was sufficient to anneal our samples adequately.

### D. Activation above 220 K

Most of the samples showed a high-temperature activation mechanism. We take it to represent a growth of topological features within the intercalate, such as vacancies, dislocations, and domain walls. If this population, $N$, is temperature activated, then

$$N/N_0 = A\,e^{-\epsilon/k_B T}\,, \qquad (5)$$

where $N_0$ is the number of molecules, $\epsilon$ is an activation temperature, $A$ is a constant representing the associated entropy, and $k_B$ is Boltzmann's constant. A plot of the logarithm of excess heat capacity versus $1/T$ will provide $\epsilon$ from the slope and $N/N_0$ from the intercept of the curve (see Christy for a similar analysis on silver bromide).[34] Figure 11 is an Arrhenius plot for the lower stage-3$B$ sample, where a constant (defect-free) background was subtracted. We find $\epsilon = 4100$ K and $N/N_0 \sim 9.5\%$ at 280 K. This fraction is sufficiently large that, were the extrapolation uncertainties in determining $N/N_0$ not so large, one might expect melting to occur in the vicinity of room temperature. Now the $SbCl_6^-$ $\sqrt{7}\times\sqrt{7}$ lattice has an order-disorder transition near 450 K, and there is x-ray evidence for a possible 340-K transition to a phase which is incommensurate, possibly fluid with unusually extended correlations.[16] We doubt that unintercalated $SbCl_5$ is present in our samples since all high-temperature heat-capacity signatures are smooth and continuous up through 280 K, although the bulk melting point is 276 K.[26] Butter of Antimony, $SbCl_3$, melts at 346 K, which is quite close to the correlated fluid transition temperature. The activation temperature, of 4100 K, however, is considerably more than the $\approx$1050-K (1530-K) latent heat of melting in $SbCl_5$ ($SbCl_3$). It is also substantially less than the heat of vaporization (5400—6600 K) for these compounds.[26] We were unable to locate any well-depth-energy calculations for antimony pentachloride or other chloride compounds, either in or adsorbed on graphite for comparison to $\epsilon$. We suspect that the activation mechanism is associated with $SbCl_3$-island sublimation rather than with the $SbCl_6^-$-$\sqrt{7}\times\sqrt{7}$ transition, which is way above room temperature. A similar analysis was performed for the stage-4$B$-(1) and stage-6 samples, giving $\epsilon = 3400$ and 1850 K, respectively. These values of $\epsilon$ are insensitive to changing the high-$T$ background subtraction from a constant value to the $SbCl_5$ vibrational fit. The lowering of $\epsilon$ with stage represents a diminishing $c$-axis interaction of $SbCl_3$ molecules as the intercalant layers grow farther apart.

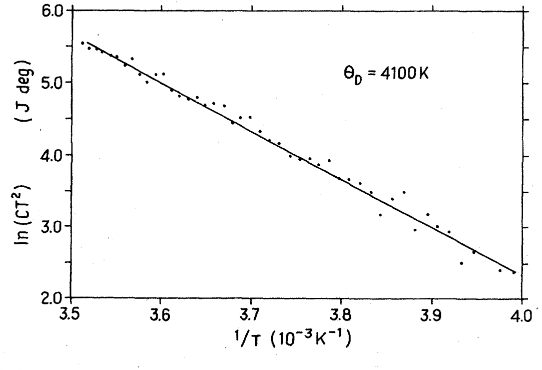

FIG. 11. Arrhenius plot for the stage-3$B$-(1) data at $T > 250$ K.

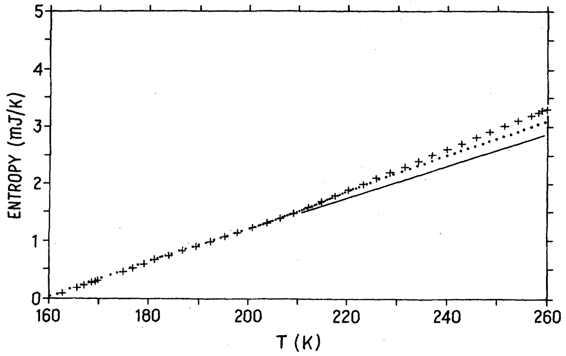

FIG. 12. Entropy-vs-temperature plot of the stage-2-(4) data while warming (·) and cooling (+). Straight line is an extrapolation of the lower-$T$ entropy.

### E. 220-K phase transition

We calculated the entropy jump in passing through the 220-K phase transition. Entropy versus temperature is plotted in Fig. 12 for the stage-2$C$-(4) sample. Linear extrapolation of the low-temperature entropy gives a specific entropy increase of $S/Nk_B = 0.8$ upon warming and 1.1 upon cooling. The respective values for sample 3 are 0.7 and 1.1. These entropies are comparable to the configurational entropy change of ln2 for a two-component-alloy order-disorder transition on a square lattice,[35] but not for $\sqrt{7}\times\sqrt{7}$ or $\sqrt{39}\times\sqrt{39}$ melting, which involves a very large number of different configurations. It is entirely possible that only a fraction of the lattice disorders or that the process is only partially completed, as suggested by the hysteresis, in which case the full specific entropy jump could be much larger. As mentioned earlier, the in-plane x-ray scans of stage 2$C$-(3) showed $\sqrt{39}\times\sqrt{39}$ peaks at room temperature (which remained unchanged after several months), while lower-temperature scans showed no unusual intensity changes in these peaks. If the 220-K transition is related to $SbCl_3$ disordering, as has been recently suggested,[8] then our x-ray measurements are evidence of an incomplete disordering process in the particular samples prepared by liquid immersion (Fig. 9).

We suspect that the first-order transition appears in our one-zone-prepared samples because they are more uniformly intercalated than the two-zone-prepared samples. We note that the specific-heat values on either side of the transition are close to the specific heats for the group-$B$ plateaus. Thus, the configurational changes in group-$C$ samples are the *same* as those in group $B$ which occur over an extended temperature interval. Group-$A$ samples appear to be more or less featureless.

## IV. CONCLUSIONS

We have explored the thermal activity of several $SbCl_5$ GIC's between 10 K and room temperature. These are physically complicated compounds whose properties depend sensitively on preparation procedures. The samples have been grouped into three categories which we believe help to highlight these inherent differences. Several probable mechanisms have been suggested for the diverse thermal activity. We realize that alternative interpretations are possible and encourage modeling calculations and comparisons with other related measurements.

Our conclusions are as follows:

(1) The specific-heat trends generally agree with degeneracies of the bulk $SbCl_5$ vibrational-mode calculations. A strong correlation to staging is apparent, with the degeneracy decreasing as stage increases.

(2) The low-temperature specific heat is significantly larger than these calculations, with the excess possessing Schottky-type thermal behavior. A stage-2 sample does appear to show the anticipated phonon behavior below 20 K.

(3) The Schottky heat-capacity peak shifts strongly to higher $T$ with stage, but disappears altogether by stage 6. We do not understand this feature.

(4) Plateau formation in group-$B$ samples is interpreted as dimer rotational unbinding. The dipoles of $SbCl_3$ start to rotate with respect to the graphite mosaic and to each other above 150 K, and begin to melt at the 220-K transition. A 150-K feature has not been reported previously.

(5) The group-$C$ samples demonstrate that this breakup can occur abruptly as a first-order process with an entropy gain of about ln2. Since $\sqrt{39}\times\sqrt{39}$ peaks were seen for one of these samples at room temperature, we know that partial melting does occur with high-temperature stability.

(6) Most samples display a distinct activation process above the 220-K transition which we attribute to topological growth. The activation energies are strongly stage dependent, suggestive of significant $c$-axis correlation.

## ACKNOWLEDGMENTS

We appreciate help from Hitoshi Homma in sample preparation and x-ray analysis. Roy Clarke made several important suggestions and contributed a close critical reading of the manuscript. We thank Hee Bak Chae and Joe Gray for technical assistance, and the National Science Foundation for support during early phases of this project.

---

[*] Present address: Department of Physics, University of Florida, Gainesville, FL 32611.

[1] W. Rudörff, Adv. Inorg. Chem. Radiochem. **1**, 233 (1959).

[2] S. A. Safran, Synth. Met. **2**, 1 (1980).

[3] J. Mélin and A. Hérold, Carbon **13**, 357 (1975).

[4] J. Mélin and A. Hérold, C. R. Acad. Sci. **269**, 877 (1969); V. K. R. Murthy, D. C. Smith, and P. C. Eklund, Mater. Sci. Eng. **45**, 77 (1980).

[5] P. C. Eklund, J. Giergiel, and P. Boolchand, in *Physics of Intercalation Compounds,* Vol. 38 of Springer Series in *Solid State Sciences,* edited by L. Pietronero and E. Tosatti (Springer, Berlin, 1980), p. 168. Also see earlier Mössbauer work by J. E. Ballard and T. Birchall, J. Chem. Soc. Dalton Trans. No. 18, 1859 (1976).

[6] M. H. Boca, M. L. Saylors, D. S. Smith, and P. C. Eklund, Synth. Met. **6**, 3306 (1983).

[7] H. Fuzellier, J. Mélin, and H. Hérold, Carbon **15**, 45 (1977).

[8] Roy Clarke, M. Elzinga, J. N. Gray, H. Homma, D. T. Morelli, M. J. Winokur, and C. Uher, Phys. Rev. B **26**, 5250 (1982).

[9] R. Clarke and H. Homma, in *Intercalated Graphite,* edited by M. S. Dresselhaus, G. Dresselhaus, J. E. Fischer, and M. J. Moran (Elsevier, New York, 1983), p. 3.

[10] G. Timp, M. S. Dresselhaus, L. Salamanca-Riba, A. Erbil, L. W. Hobbs, G. Dresselhaus, P. C. Eklund, and Y. Iye, Phys. Rev. B **26**, 2323 (1982).

[11] P. C. Eklund, E. R. Falardeau, and J. E. Fischer, Solid State Commun. **32**, 631 (1979).

[12] P. C. Eklund, D. S. Smith, and V. R. K. Murthy, Synth. Met. **2**, 99 (1980).

[13] M. Elzinga, D. T. Morelli, and C. Uher, Phys. Rev. B **26**, 3312 (1982).

[14] M. S. Dresselhaus and G. Dresselhaus, Adv. Phys. **30**, 139 (1981); S. A. Solin, Adv. Chem. Phys. **49**, 455 (1982).

[15] D. N. Bittner, Ph.D. thesis, University of Michigan, 1984.

[16] H. Homma, Ph.D. thesis, University of Michigan, 1984.

[17] T. Rayment, R. Schlogl, and J. M. Thomas, Phys. Rev. B **30**, 1034 (1984).

[18] P. F. Sullivan and G. Seidel, in Proceedings of 1966 Low $T$ Calorimetry Conference, Otaniemi, Finland, edited by O. V. Lounasmaa [Ann. Acad. Sci. Fenn. A **210** (1966)]. See also Phys. Rev. **173**, 679 (1968).

[19] I. Hatta and A. J. Ikushima. Jpn. J. Appl. Phys. **20**, 1995 (1981).

[20] S. M. Dockerty, Can. J. Res. **9**, 84 (1933); **15A**, 59 (1937); B. M. Boerstoel, W. J. J. Van Dissel, and M. B. M. Jacobs, Physica (Utrecht) **38**, 287 (1968).

[21] P. H. Keesom and N. Pearlman, Phys. Rev. **99**, 1119 (1955).

[22] H. Homma and R. Clarke, Phys. Rev. Lett. **52**, 629 (1984).

[23] See, for instance, P. M. A. Sherwood, *Vibrational Spectroscopy of Solids* (Cambridge University Press, London, 1972).

[24] I. R. Beattie and G. A. Ozin, J. Chem. London, Sec. A, 1691 (1969).

[25] J. K. Wilmshurst, J. Mol. Spectrosc. **5**, 343 (1960).

[26] *Gmelin Handbook of Inorganic Chemistry—Antimony* (Gmelin, Heidelberg, West Germany, 1949).

[27] R. Al-Jishi and G. Dresselhaus, Phys. Rev. B **26**, 4523 (1982).

[28] U. Mizutani, T. Kondow, and T. B. Massalski, Phys. Rev. B **17**, 3165 (1978).

[29] M. Suganuma, T. Kondow, and U. Mizutani, Phys. Rev. B **23**, 706 (1981).

[30] M. G. Alexander, D. P. Goshorn, and D. G. Onn, Phys. Rev. B **22**, 4535 (1980).

[31] P. C. Eklund, V. Yeh, H. G. Smith, R. Nicklow, R. Al-Jishi, and G. Dresselhaus, Phys. Rev. B **29**, 2138 (1984).

[32] R. W. Wang, H. Taub, H. Shechter, R. Brener, J. Suzanne, and F. Y. Hansen, Phys. Rev. B **27**, 5864 (1983); R. W. Wang, Ph.D. thesis, University of Missouri—Columbia, 1983.

[33] D. M. Hwang and G. Nicolaides, Solid State Commun. **49**, 483 (1984).

[34] R. W. Christy and A. W. Lawson, J. Chem. Phys. **19**, 517 (1951).

[35] See, for example, K. Huang, *Statistical Mechanics* (Wiley, New York, 1963), p. 48.